Forward-Looking MIMO-SAR for Enhanced Angular Resolution

Adnan Albaba
ETRO - VUB
Imec Leuven
Leuven, Belgium
Adnan.Albaba@imec.be

Adham Sakhnini
ESAT - KU Leuven
Imec Leuven
Leuven, Belgium
Adham.Sakhnini@imec.be

Hichem Sahli
ETRO - VUB
Imec Leuven
Leuven, Belgium
Hichem.Sahli@imec.be

André Bourdoux
Imec Leuven
Leuven, Belgium
Andre.Bourdoux@imec.be

***Abstract*—This paper analyzes the monostatic forward-looking synthetic aperture radar (FL-SAR) imaging problem. A frequency-modulated continuous wave (FMCW) signal model for the FL single input single output (SISO) SAR (FL-SISO-SAR) problem is presented. The FL-SISO-SAR model is then extended to the FL multiple input multiple output (MIMO) SAR (FL-MIMO-SAR). In both cases, the spatial dependence of the Doppler information along the travel path is exploited by means of Doppler beam sharpening (DBS). In addition to enhancing the angular resolution, the proposed method significantly suppresses the grating lobes. Finally, a simple method for reducing the computational complexity of the FL-SISO-SAR and the FL-MIMO-SAR, using slow-time decimation with fast-time backprojection, is introduced. Simulation results for four different scenarios are presented. The results show a good angular resolution using the FL-SISO-SAR. Moreover, the FL-MIMO-SAR results in a more refined angular resolution and resolves the targets at zero look-angle, which is a fundamental limitation of DBS. In addition, the FL-MIMO-SAR suppresses the grating lobes, which are due to the large antenna spacing.**

***Index Terms*—Radar imaging, FL-SAR, DBS, synthetic aperture radar, angular resolution, MIMO, complexity reduction, backprojection, grating lobe suppression**

I. Introduction

For radar imaging applications, high range, Doppler, and angular resolution are required [1]. While better range and Doppler resolution can be achieved with larger bandwidth and longer observation time, respectively, higher angular resolution is achieved with larger antenna apertures, which can be expensive or infeasible. To circumvent this problem, the concept of synthetic aperture radar (SAR) [2] can be used when the geometry allows.

Synthetic apertures are formed by collecting snapshots along the travel path, exploiting the platform motion. A typical automotive example is a side-looking (SL) SAR for parking assistance [3]. However, in the case of a forward-looking (FL) radar, the geometry is different since the vehicle moves towards the imaged scene instead of passing alongside it. One way to tackle the FL-SAR imaging problem is to exploit an additional (or a different) motion component of the platform (or the radar). This yields a synthetic aperture of three or more dimensions, which is referred to as Volumetric SAR, see [4]. Gishkori, et al. [5], used a scanning phased array radar, incorporating the scene scanning along the cross-range of interest, for FL automotive radar imaging (i.e. forward scanning). Wang, et al. [6], exploited the radial scanning for a ground penetrating radar imaging (i.e. Elevation-radial scanned SAR). Nguyen, et al. [7], employed a gliding-down path of a rotor aircraft, which forms a depression angle with respect to the scene center. The depression angle varies along the cross-range due to the forward motion of the rotor aircraft. Another way to solve the FL-SAR imaging problem would be to use bistatic SAR configurations. Meng, et al. [8], considered a missile-borne bistatic forward-looking SAR towards target detection, recognition, and tracking. Espeter, et al. [9], demonstrated for the first time a spaceborne-airborne forward-looking bistatic SAR experiment.

The Doppler beam sharpening (DBS) method (the frequency-domain SAR [2]) can also be used as a solution for the FL-SAR imaging problem. It utilises the variations in the relative Doppler frequency shift of scatterers at different look-angles with respect to the trajectory of a radar. Daniel, et al. [10], investigated the application of DBS for the angular resolution refinement of low-terahertz radar sensing. Laribi et al. [11], exploited DBS together with the three dimensional high resolution RELAX algorithm for estimating the height of extended objects. In addition, Yang et al. [12], combined DBS with the fast iterative adaptive approach to achieve the high azimuth resolution in the forward-squint region. However, the conventional DBS-based imaging approaches have no or poor angular resolution for look angles equal or close to zero degree.

In this paper, we propose a solution for the monostatic FL-SAR imaging problem without incorporating any additional motion component. To achieve this, we exploit the spatial variation in Doppler information along the synthetic aperture. First, we present an Frequency-Modulated Continuous Wave (FMCW) [13] signal model for the FL single input single output (SISO) SAR (FL-SISO-SAR) problem.
Then, we extend the FL-SISO-SAR model to the FL multiple input multiple output (MIMO) SAR (FL-MIMO-SAR) case. The concept of MIMO radar [14] has been an active field of research, as it helps achieving high angular resolution with lower antenna count (compared to beamforming case). It employs the orthogonality between the TX signals and a special arrangement of the TX and RX arrays. In the

Final version: DOI: 10.1109/RadarConf2248738.2022.9764255

FL-MIMO-SAR case, the added antenna aperture (i.e. virtual antenna array) proves to tackle the limitation of zero-degree look-angle targets. In addition, the FL-MIMO-SAR can suppress the grating lobes, which result when the spacing between antenna elements exceeds half the wavelength. We study this behaviour. Finally, we employ a method for a faster implementation of the mentioned approaches by combining decimation in the slow-time domain with backprojection (BP) in the fast-time domain.

The rest of the paper is organized as follows; Section II sets up the geometry of the FL-SAR problem as well as the FMCW signal model for the FL-SISO-SAR and the FL-MIMO-SAR cases. A simple method for complexity reduction is proposed in Section III. Section IV deals with the grating lobe suppression problem. Simulation results are presented and discussed in Section V, while the conclusions are drawn in Section VI.

II. Geometry and Signal Model

Fig. 1a illustrates the 2D geometry (x-axis for down-range and y-axis for cross-range) for the FL-SISO-SAR problem. The red circles indicate specific positions of the radar, where each snapshot is captured along the travel path. The black circle indicates a scatterer S at $\{x_S, y_S\}$, which is assumed to be static. The platform, on which the radar is mounted, is assumed to be moving towards S with a constant velocity $v = \sqrt{\dot{x}^2 + \dot{y}^2}$. The motion is assumed to be on the x-axis only (i.e. $\dot{y} = 0$). x_0, x_1, and x_{N-1} denote the x-coordinates of the radar's first, second, and Nth snapshot, respectively. $\theta(n)$ and $R_S(n)$ denote the look-angle and distance, respectively, of a target for the radar at certain location n. y_T denotes the cross-range of the radar (which is constant).

A. FMCW FL-SISO-SAR

For what follows, we consider a SISO FMCW radar with the following parameters:

$$\lambda = \frac{c}{f_c}, \quad T_p = T_c + T_i + T_r, \quad \alpha = \frac{BW}{T_c}$$

where λ is the wavelength, c is the speed of light, f_c is the carrier frequency, T_p is the chirp repetition interval, T_c is the chirp duration, T_i is the chirp idle time, T_r is the chirp return time, α is the chirp slope, and BW is the bandwidth. We also define $n = 0, 1, \ldots, N$ to be the chirp index (slow time), $t_f \in [0 : T_c]$ to be the intra-chirp time (fast time), and f_s to be the baseband sampling frequency.

Following the above mentioned assumptions, the travelled distance at (n, t_f) is equal to $(x_0 + nvT_p + vt_f)$. For simplicity, we assume $x_0 = 0$. The range at (n, t_f) is then expressed as:

$$R(n, t_f) = \sqrt{(x_S - nvT_p - vt_f)^2 + (y_S - y_T)^2} \quad (1)$$

and the two way propagation delay τ at (n, t_f) is given by

$$\tau(n, t_f) = \frac{2R(n, t_f)}{c} \quad (2)$$

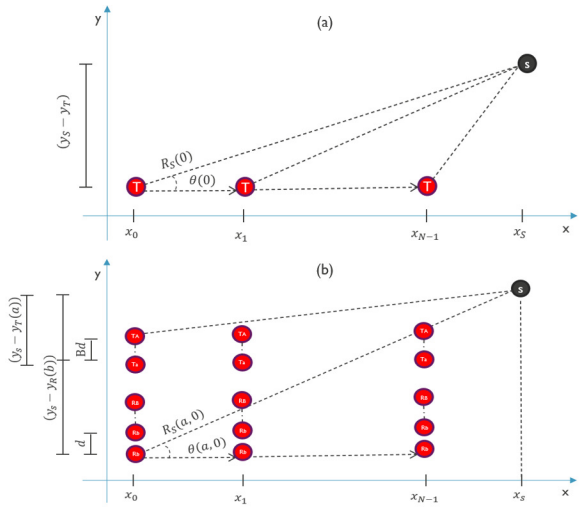

Fig. 1: The geometry of the (a) FL-SISO-SAR and (b) FL-MIMO-SAR. Explained in Section II.

The transmitted radar signal can be expressed as

$$s(t_f) = e^{i\pi\alpha t_f^2} e^{i2\pi f_c t_f} \quad (3)$$

The radar receives the echo from the scatterer after a propagation delay $\tau(n, t_f)$, and the received signal can be expressed as

$$r(t_f) = \Lambda e^{i\pi\alpha t_f^2} e^{i\pi\alpha\tau^2} e^{-i2\pi\alpha t_f \tau} e^{i2\pi f_c t_f} e^{-i2\pi f_c \tau} \quad (4)$$

where Λ is the complex amplitude term. After de-chirping, the baseband beat frequency signal is obtained and can be expressed as:

$$\zeta(t_f) = \Lambda e^{-i2\pi f_c \tau} e^{-i2\pi\alpha t_f \tau} e^{i\pi\alpha\tau^2} \quad (5)$$

The beat frequency signal can then be obtained by plugging (1) and (2) into (5). To optimize the signal-to-noise ratio (SNR), the matched filter (MF) solution is derived as

$$Z_s(l, m) = \sum_{n=1}^{N} \sum_{k=1}^{K} \zeta(n, k) \gamma(n, k, l, m) \quad (6)$$

where $\left(\frac{k}{f_s},\ k = 0, 1, \ldots, K-1\right)$ are the sampling instants. Moreover, $l = \frac{2x_S BW}{c}$ and m are the range and cross-range bin indices, respectively. $\gamma(n, k, l, m)$ is the complex conjugate of the hypothetical beat frequency signal $\zeta(n, k, l, m)$.

It is clear that the computational complexity of the solution in (6) makes it hard to be implemented in real-time. The double summation over k and n must be computed for all values of l and m, resulting in a complexity of $\mathcal{O}(LMNK)$, hence, a complexity reduction is needed.

B. FMCW FL-MIMO-SAR

For what follows, we consider a generic 1-D time-division multiplexing (TDM) MIMO FMCW radar, placed on the y-axis as illustrated in Fig. 1b, with the same parameters defined above. The MIMO array consists of A transmitters

T_a $(a = 1, 2, \ldots, A)$ and B receivers R_b $(b = 1, 2, \ldots, B)$ with spacing d between two receivers, and Bd between two transmitters. The resulting virtual array consists of $A \cdot B$ receivers with spacing d between two virtual receivers. $y_T(a)$ and $y_R(b)$ denote the cross-range of transmitter a and receiver b, respectively. In TDM-MIMO, a given transmitter T_a is active at the slow-time instants $(An + a)T_p$.

Following these definitions, the distances travelled by transmitters and receivers at (a, b, n, t_f) is equal to $(x_0 + AnvT_p + avT_p + vt_f)$. For simplicity, we assume $x_0 = 0$ which denotes the initial x-coordinate of all transmitters and receivers, see Fig. 1b. The two-way range at (a, b, n, t_f) is then expressed as:

$$\begin{aligned} &R(a, b, n, t_f) \\ &= \sqrt{(x_S - AnvT_p - avT_p - vt_f)^2 + (y_S - y_R(b))^2} \\ &+ \sqrt{(x_S - AnvT_p - avT_p - vt_f)^2 + (y_S - y_T(a))^2} \end{aligned} \tag{7}$$

With $\tau(a, b, n, t_f) = \frac{R(a,b,n,t_f)}{c}$, and by following the steps (3)-(5), the MF solution for the MIMO case can be expressed as:

$$Z_m(l, m) = \sum_{a=1}^{A} \sum_{b=1}^{B} \sum_{n=1}^{N} \sum_{k=1}^{K} \zeta(a, b, n, k) \gamma(a, b, n, k, l, m) \tag{8}$$

The computational complexity of the solution in (8) is $\mathcal{O}(LMNKAB)$, hence, a complexity reduction is needed.

C. Angular Resolution

The angular resolution $\Delta\theta$ for the case of a single snapshot constraint (i.e. no SAR is applied) can be given as follows:

$$\Delta\theta \approx \frac{\lambda}{D} \tag{9}$$

where D denotes the aperture size. If FL-SAR is considered, the refined DBS-based angular resolution $\Delta\theta_{DBS}$ can be given as follows, see [10] for a complete derivation:

$$\Delta\theta_{DBS} = \frac{\lambda}{2\dot{x}T_p N \sin(\theta)} \tag{10}$$

where, θ is the look-angle. Note the $\sin(\theta)$ in the denominator of the expression (10). This means that in the case of targets at zero look-angle, no angular refinement can be provided which is a fundamental limitation of DBS.

In the case of FL-MIMO-SAR, the angular resolution will be contributed by both phenomena (i.e. resolution by (9) and (10)), with the best of two being approximately the effective angular resolution. For example, in the case of FL-MIMO-SAR with a target at zero look-angle, the angular resolution will be governed by (9) and not (10). These statements will be validated in Section V.

III. Complexity Reduction

As mentioned in the previous sections, the MF solutions for the SISO (6) and MIMO (8) cases are inapplicable for real-time applications due to their complexity.

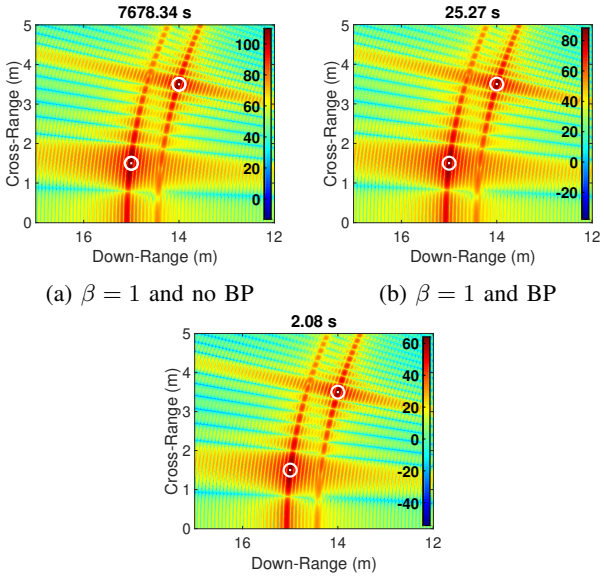

(a) $\beta = 1$ and no BP (b) $\beta = 1$ and BP

(c) $\beta = 13$ and BP

Fig. 2: A comparison between FL-SISO-SAR MF (a) where no decimation or BP is applied, BP-based FL-SISO-SAR (b) where BP is applied but with no decimation, and Dec-BP-based FL-SISO-SAR (c) with decimation factor β of 13 and BP. Targets at (15,1.5)m and (14,3.5)m, marked with white circles with crosses in the middle.

One way to reduce the computational complexity is to decimate one or both of the fast-time and slow-time sample domains. To avoid aliasing and SNR loss, due to decimation, a low-pass filter (LPF) is implemented prior to the decimation step. We can then reconstruct within a reduced alias-free down-sampled field of view (FOV).

First, we define the alias-free cross-range FOV of interest (i.e. $\arctan\left(\frac{\max(y_S)}{\min(x_S)}\right)$). Then, based on the definition of the maximum alias-free cross-range extent [15], the decimation factor β is obtained as follows:

$$\beta = \frac{N^2\lambda}{2\arctan(\frac{\max(y_S)}{\min(x_S)})T_p} \tag{11}$$

Lastly, a finite impulse response LPF is applied to the slow-time sample set prior to the decimation.

To reduce the complexity even more, the BP method is used, by applying an inverse fast Fourier transform (*IFFT*), for up chirps, along the zero-padded fast-time domain. This is followed by a linear interpolation on the *IFFT* output. Finally, a phase correction step is applied and the slow-time samples are coherently added [15].

This combination of slow-time decimation and fast-time BP (Dec-BP) yields a reduced computational complexity of $\mathcal{O}(LM\hat{N}\log(K))$ for (6) as well as $\mathcal{O}(LM\hat{N}\log(K)AB)$ for (8), where $\hat{N} = N/\beta$.

To demonstrate the usability and speed of the Dec-BP approach, we consider 2 point targets at positions (15,1.5)m

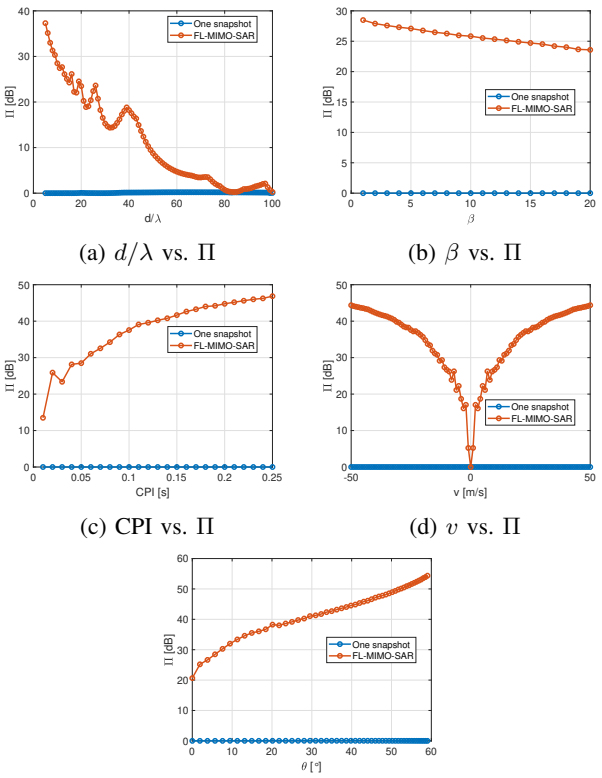

(a) d/λ vs. Π (b) β vs. Π

(c) CPI vs. Π (d) v vs. Π

(e) θ vs. Π

Fig. 3: Effects of the choice of different parameters (d, β, CPI, v, and θ) on the grating lobe suppression performance Π.

and (14,3.5)m. Fig. 2 illustrates the resulting 2D maps (in dB scale). Fig. 2a depicts the resulting image using a FL-SISO-SAR MF with no decimation (i.e. $\beta = 1$) and no BP, which takes 7678.34s to compute. On the other hand, the computation time was drastically decreased to 25.27s using the BP-based FL-SISO-SAR MF (see Fig. 2b), with no decimation. Fig. 2c shows the results using the Dec-BP-based FL-SISO-SAR MF, with decimation factor of 13 (reduces the FoV to $\pm 23°$), which reduces the computational time to 2.08s. This decimation factor was determined using (11).

IV. Suppression of Grating Lobes

A grating lobe can be identified as a spatial aliasing or a replica of the main lobe but in a wrong location, which results from the large spacing between antennas (i.e. $d > \frac{\lambda}{2}$). Despite not affecting the resolution, the impact of grating lobes on the quality of the image is significant, hence grating lobes must be suppressed. To determine the angles ϕ of the grating lobes for a true target at angle θ, the following equation is used:

$$\phi(g) = \arcsin\left(\frac{g2\pi + \sin(\theta)\frac{2\pi d}{\lambda}}{2\pi} \times \frac{\lambda}{d}\right) \tag{12}$$

where $g = \pm 1, \pm 2, \ldots, \pm G - 1$, and $G = \frac{2d}{\lambda}$, keeping only the acceptable (i.e. real) values in (12).

Our simulations, see Section V, show that the proposed FL-MIMO-SAR approach, with large inter-element spacing,

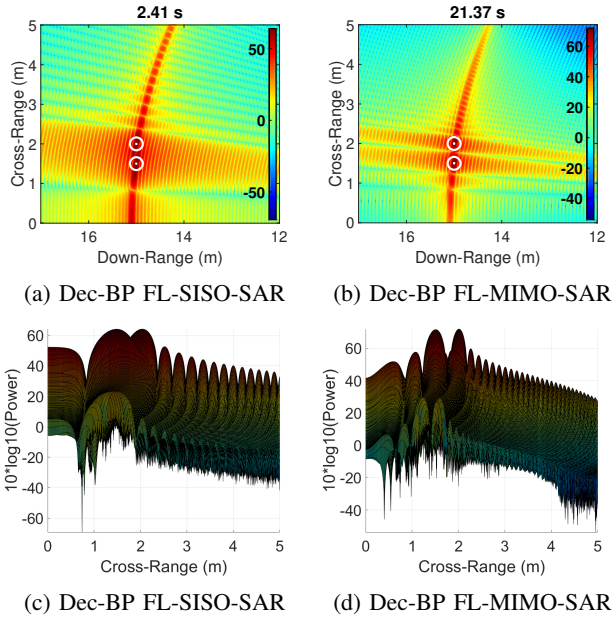

(a) Dec-BP FL-SISO-SAR (b) Dec-BP FL-MIMO-SAR

(c) Dec-BP FL-SISO-SAR (d) Dec-BP FL-MIMO-SAR

Fig. 4: Scenario 1: White circles indicate true target positions. (a) and (c) Dec-BP FL-SISO-SAR with $\beta = 13$. (b) and (d) Dec-BP FL-MIMO-SAR with $\beta = 13$.

manages to suppress the resulting grating lobes. To quantitatively analyze this behaviour, we use the performance index Π, which is the ratio between the power of the main lobe to the power of the grating lobe. The fact that θ in (12) is function of (a, b, n, k) enables us to study the relation between Π and other design parameters (e.g. d and v) such that:

$$\Pi(a, b, n, k) = 10 \log\left(\frac{\left|Z_m\Big(\theta(a, b, n, k)\Big)\right|^2}{\left|Z_m\Big(\phi(\theta(a, b, n, k), g)\Big)\right|^2}\right) \tag{13}$$

Fig. 3 illustrates the relation between 5 different parameters with the grating lobe suppression performance index Π in the case of one true target at $\theta = 3.8°$, for the first 4 sub-figures, and for $g = 1$. For each sub-figure, one parameter is varied while fixing the others, see the fourth scenario experiment in Section V for the parameters' values and antenna settings. It is obvious that, for the case of a MIMO radar with large d, the grating lobes are not suppressed and have amplitudes approximately equal to the main lobe (i.e. $\Pi = 0$ dB) in the case of one snapshot. However, the FL-MIMO-SAR shows good performance in suppressing the grating lobes (i.e. $\Pi > 0$ dB) depending on the choice of the parameters. This is due to the fact that the Doppler phase history for a target is different from one virtual array element to another, and this difference becomes significant for large virtual antenna apertures. Therefore, the grating lobes are suppressed in the FL-MIMO-SAR.

Π degrades when d is increased because this also increases the inter-element spacing (Fig. 3a). Hence, the first grating is closer to the true target angle and its phase history is more

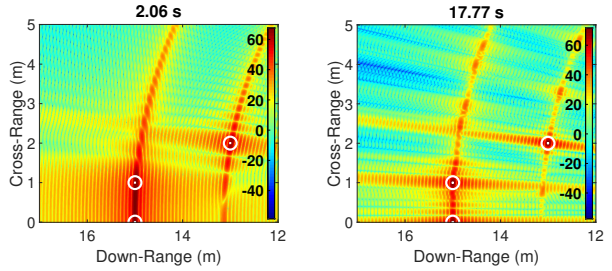

(a) Dec-BP FL-SISO-SAR (b) Dec-BP FL-MIMO-SAR

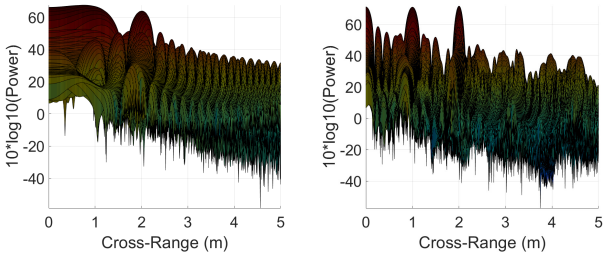

(c) Dec-BP FL-SISO-SAR (d) Dec-BP FL-MIMO-SAR

Fig. 5: Scenario 2: White circles indicate true target positions. (a) and (c) Dec-BP FL-SISO-SAR with $\beta = 13$. (b) and (d) Dec-BP FL-MIMO-SAR with $\beta = 13$.

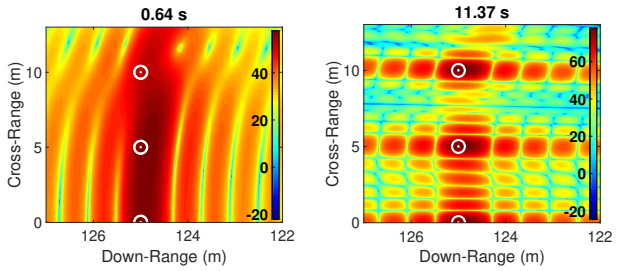

(a) Dec-BP FL-SISO-SAR (b) Dec-BP FL-MIMO-SAR

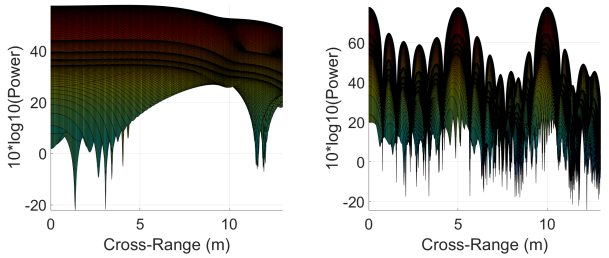

(c) Dec-BP FL-SISO-SAR (d) Dec-BP FL-MIMO-SAR

Fig. 6: Scenario 3: White circles indicate true target positions. (a) and (c) Dec-BP FL-SISO-SAR with $\beta = 45$. (b) and (d) Dec-BP FL-MIMO-SAR with $\beta = 45$.

similar. It appears that for an increase in β a small degradation in Π is expected (Fig. 3b). On the other hand, Π improves for increasing coherent processing interval (CPI) (at constant v) or increasing v (at constant N), regardless of the direction (Fig. 3c and Fig. 3d). Lastly, Fig. 3e shows that the grating lobe suppression improves for increasing target angle. Overall, the plots in Fig. 3 can be used as guidelines to tune the parameters for optimum grating lobe reduction.

V. Results and Discussion

Simulation results were produced using the following parameters: $f_c = 79$ GHz, $BW = 2$ GHz (for $R = 15$ m) or $BW = 0.25$ GHz (for $R = 125$ m), $f_s = 6.25$ MHz, $v = 10$ m/s, $T_p = 40\ \mu s$, CPI = 50 ms, $N = 1250$, and $K = 250$. The PC used to run the simulations has a 1.90 GHz Intel(R) Core(TM) i5-8365U CPU with 16.0 GB RAM. In the following simulation scenarios, we focus on the elevation as the cross-range of interest. It is worth noting that no windowing or filtering was applied.

Four different scenarios where evaluated. In all scenarios, the MIMO array used is a generic 1-D TDM-MIMO. Table I shows the number of point targets and their locations as well as the MIMO array configuration in each scenario. Fig. 4 to Fig. 7 illustrate the resulting 2D maps and their corresponding cross-range cuts (all in dB scale) for the four scenarios, respectively. The white circles, with crosses in the middle, on the 2D maps indicate the ground truth, and the computation time is indicated in the upper caption of the sub-figures.

By comparing the sub-figures in Fig. 4, it is clear that the FL-SISO-SAR method produces good angular resolution.

TABLE I: Scenario parameters: MIMO topology and target (x,y) positions

Scenario	Target 1	Target 2	Target 3	Tx	Rx	d
1	(15,1.5)m	(15,2)m	-	2	4	$\frac{\lambda}{2}$
2	(15,0)m	(15,1)m	(13,2)m	2	4	10λ
3	(125,0)m	(125,5)m	(125,10)m	4	4	10λ
4	(15,1.5)m	(15,2.5)m	-	2	4	10λ

Moreover, it can be seen that the FL-MIMO-SAR results in a better angular resolution compared to the SISO case.

As expected, the FL-SISO-SAR produces very poor angular resolution for look-angles equal or close to zero, see Fig. 5a and Fig. 5c. This is because of the $\sin(\theta)$ in the denominator of the expression (10). This problem was solved using the FL-MIMO-SAR as shown in Fig. 5b and Fig. 5d.

In the third scenario experiment, we increased the down-range to 125m. The results from FL-SISO-SAR showed no angular resolution due to the very low look-angles as shown in Fig. 6a and Fig. 6c. On the other hand, the FL-MIMO-SAR succeeded in resolving the three targets as depicted in Fig. 6b and Fig. 6d.

Lastly, the fourth scenario experiment illustrates the robustness of the FL-MIMO-SAR against grating lobes, which are due to larger spacing between antennas (i.e. $d > \frac{\lambda}{2}$) as seen in Fig. 7. Indeed, by using (12), we expected the grating lobes to show at cross-ranges 0, 0.97, 3.05, 4.11, and 4.71m within our FOV in the case of one snapshot MIMO, see Fig. 7a and Fig. 7c (marked with black arrows). These grating lobes were suppressed when using the FL-MIMO-SAR as depicted in Fig. 7b to Fig. 7d.

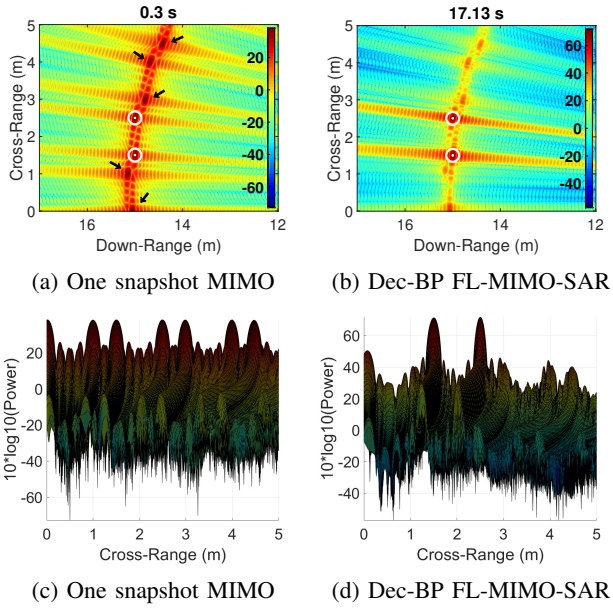

(a) One snapshot MIMO (b) Dec-BP FL-MIMO-SAR

(c) One snapshot MIMO (d) Dec-BP FL-MIMO-SAR

Fig. 7: The resulting grating lobes due to sub-wavelength antenna spacing (Scenario 4): White circles indicate true target positions. The grating lobes are marked with black arrows: (a) and (c) MIMO one snapshot taken at (0,0). (b) and (d) Dec-BP FL-MIMO-SAR with $\beta = 13$.

It is worth mentioning that the DBS-based approach cannot discriminate between positive and negative angles, which leads to a mirroring effect around $0°$.

VI. Conclusion

An FMCW signal model for the FL-SISO-SAR problem and the FL-MIMO-SAR was presented, which allowed us to derive the MF for both cases. Moreover, we proposed a method for reducing the computational complexity of the FL-SISO-SAR and the FL-MIMO-SAR. An analysis of the angular resolution of the DBS and widely spaced MIMO showed the potential in improving the angular resolution with a combined approach (i.e. FL-MIMO-SAR).

Simulation results showed good angular resolution using the FL-SISO-SAR. Moreover, the FL-MIMO-SAR resulted in a more refined angular resolution compared to the FL-SISO-SAR case. For targets at zero look-angle, the FL-SISO-SAR has very poor angular resolution, which was solved using the FL-MIMO-SAR, thanks to the large aperture size. However, the large inter-element spacing led to grating lobes, which were suppressed thanks to the combination of DBS and large aperture size.

Currently, the presented work is limited by the following factors, which will be addressed in future work: 1) no source of noise or interference was added to the model or the simulations; 2) faster FL-MIMO-SAR image reconstruction is needed for real-time applications; 3) 3D model, platform motion in cross-range, and moving targets were not considered; 4) the discrimination between positive and negative angles with the DBS-based approach was not considered; 5) developing a hardware allowing signal distribution over a physically large array.

References

[1] S. M. Patole, M. Torlak, D. Wang, and M. Ali, "Automotive radars: A review of signal processing techniques," IEEE Signal Processing Magazine, vol. 34, no. 2, pp. 22–35, 2017.

[2] C. A. Willey, "Synthetic aperture radars–a paradigm for technology evolution," IEEE Transactions on Aerospace and Electronic Systems, vol. 21, no. 3, pp. 440-443, 1985.

[3] R. Feger, A. Haderer, and A. Stelzer, "Experimental verification of a 77-GHz synthetic aperture radar system for automotive applications." IEEE MTT-S International Conference on Microwaves for Intelligent Mobility (ICMIM), pp. 111-114, IEEE, 2017.

[4] C. F. Barnes and S. Prasad, "In Situ Volumetric SAR," in IEEE Transactions on Geoscience and Remote Sensing, vol. 56, no. 10, pp. 6082-6100, Oct. 2018, doi: 10.1109/TGRS.2018.2831644.

[5] S. Gishkori, L. Daniel, M. Gashinova, and B. Mulgrew, "Imaging for a forward scanning automotive synthetic aperture radar," IEEE Transactions on Aerospace and Electronic Systems, vol. 55, no. 3, pp.1420-1434, 2018.

[6] J. Wang and A. Yarovoy, "Forward-Looking GPR Imaging with Near-Optimal 3-D Synthetic Array," 2019 13th European Conference on Antennas and Propagation (EuCAP), pp. 1-4, 2019.

[7] L.H. Nguyen and C. Le, "3D imaging for millimeter-wave forward-looking synthetic aperture radar (SAR)," Passive and Active Millimeter-Wave Imaging XXIII, Vol. 11411, p. 114110K. International Society for Optics and Photonics, 2020.

[8] Z. Meng, Y. Li, S. Zhu, Y. Quan, M. Xing, and Z. Bao, "MIMO-based forward-looking SAR imaging algorithm and simulation," International Journal of Antennas and Propagation, 2014.

[9] T. Espeter, I. Walterscheid, J. Klare, A. R. Brenner and J. H. G. Ender, "Bistatic Forward-Looking SAR: Results of a Spaceborne–Airborne Experiment," in IEEE Geoscience and Remote Sensing Letters, vol. 8, no. 4, pp. 765-768, July 2011, doi: 10.1109/LGRS.2011.2108635.

[10] L. Daniel, A. Stove, E. Hoare, D. Phippen, M. Cherniakov, B. Mulgrew, M. Gashinova, "Application of Doppler beam sharpening for azimuth refinement in prospective low-THz automotive radars," IET Radar, Sonar & Navigation, vol. 12, no. 10, pp. 1121-1130, 2018.

[11] A. Laribi, M. Hahn, J. Dickmann and C. Waldschmidt, "A new height-estimation method using FMCW radar Doppler beam sharpening," 2017 25th European Signal Processing Conference (EUSIPCO), 2017, pp. 1932-1396, doi: 10.23919/EUSIPCO.2017.8081546.

[12] H. Yang, D. Mao, Y. Zhang, Y. Zhang, Y. Huang and J. Yang, "Doppler beam sharpening imaging based on fast iterative adaptive approach," 2017 IEEE Radar Conference (RadarConf), 2017, pp. 1419-1423, doi: 10.1109/RADAR.2017.7944429.

[13] M. Skolnik, "Radar Handbook," McGraw-Hill Education, 2008.

[14] E. Fishler, A. Haimovich, R. Blum, D. Chizhik, L. Cimini and R. Valenzuela, "MIMO radar: An idea whose time has come," Proc. IEEE Radar Conf., pp. 71-78, 2004-Apr.

[15] L. A. Gorham and L. J. Moore, "SAR image formation toolbox for MATLAB," Algorithms for Synthetic Aperture Radar Imagery XVII, Vol. 7699, p. 769906, International Society for Optics and Photonics, 2010, doi: 10.1117/12.855375.